Bioconjugate Chemistry

Article

Cite This: Bioconjugate Chem. 2019, 30, 1821−1829

pubs.acs.org/bc

An Albumin-Binding T_1-T_2 Dual-Modal MRI Contrast Agents for Improved Sensitivity and Accuracy in Tumor Imaging

Zijian Zhou,[†] Ruiliang Bai,[*,‡] Zhantong Wang,[†] Henry Bryant,[□] Lixin Lang,[†] Hellmut Merkle,[Δ] Jeeva Munasinghe,[Δ] Longguang Tang,[†] Wei Tang,[†] Rui Tian,[†] Guocan Yu,[†] Ying Ma,[†] Gang Niu,[†] Jinhao Gao,[*,§] and Xiaoyuan Chen[*,†]

[†]Laboratory of Molecular Imaging and Nanomedicine, National Institute of Biomedical Imaging and Bioengineering, National Institutes of Health, Bethesda, Maryland 20892, United States

[‡]Interdisciplinary Institute of Neuroscience and Technology, Qiushi Academy for Advanced Studies, Key Laboratory of Biomedical Engineering of Ministry of Education, College of Biomedical Engineering and Instrument Science, Zhejiang University, Hangzhou 310027, China

[□]Laboratory of Diagnostic Radiology Research, Radiology and Imaging Sciences, Clinical Center, National Institutes of Health, Bethesda, Maryland 20892, United States

[Δ]Laboratory of Functional and Molecular Imaging, National Institute of Neurological Disorders and Stroke, National Institutes of Health, Bethesda, Maryland 20892, United States

[§]State Key Laboratory of Physical Chemistry of Solid Surfaces, The MOE Key Laboratory of Spectrochemical Analysis and Instrumentation, The Key Laboratory for Chemical Biology of Fujian Province, Department of Chemical Biology, College of Chemistry and Chemical Engineering, Xiamen University, Xiamen 361005, China

Supporting Information

ABSTRACT: Magnetic resonance imaging (MRI) diagnosis is better assisted by contrast agents that can augment the signal contrast in the imaging appearance. However, this technique is still limited by the inherently low sensitivity on the recorded signal changes in conventional T_1 or T_2 MRI in a qualitative manner. Here, we provide a new paradigm of MRI diagnosis using T_1-T_2 dual-modal MRI contrast agents for contrast-enhanced postimaging computations on T_1 and T_2 relaxation changes. An albumin-binding molecule (i.e., truncated Evans blue) chelated with paramagnetic manganese ion was developed as a novel T_1-T_2 dual-modal MRI contrast agent at high magnetic field (7 T). Furthermore, the postimaging computations on T_1-T_2 dual-modal MRI led to greatly enhanced signal-to-noise ratios (SNR) and contrast-to-noise ratios (CNR) in both subcutaneous and orthotopic brain tumor models compared with traditional MRI methods. The T_1-T_2 dual-modal MRI computations have great potential to eliminate suspicious artifacts and false-positive signals in mouse brain imaging. This study may open new avenues for contrast-enhanced MRI diagnosis and holds great promise for precision medicine.

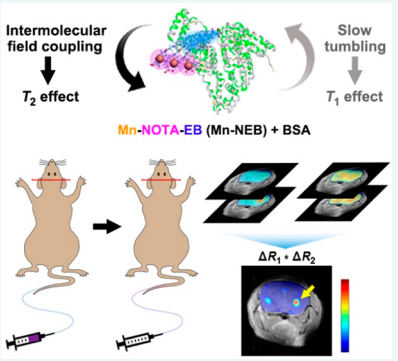

INTRODUCTION

Precision medicine relies heavily on applicable diagnosis that can provide distinct and accurate pathological characteristics for individuals.[1−3] A handful of molecular imaging tools are available in modern medicine, such as positron emission tomography (PET) and magnetic resonance imaging (MRI). These imaging techniques play important roles in assisting disease diagnosis in the clinic; however, they all have their own intrinsic merits and drawbacks.[4,5] For example, PET has outstanding radiotracer sensitivity but is limited by the poor anatomical and structural comprehension, whereas MRI can provide exquisite soft tissue contrast with high spatial-temporal resolution but with relatively low sensitivity. To yield an accurate diagnosis, multiple imaging results from different machines are often required, which burden patients in both economic cost and mentality.[6,7] Although combination imaging instruments are clinically available, it is still challenging to compare diagnostic information across different imaging modalities because of the unparalleled spatial-temporal resolutions with different imaging mechanisms.[8−10] Therefore, it is highly desirable to develop a new imaging program that can provide multiparametric images for improving disease diagnosis and treatment decision-making.[11−14]

MRI is one of the most widely used clinical imaging tools because of its noninvasive, nonionized, and radiation-free characteristics. Contrast agents are used in approximately 40% of MRI studies in the clinic.[15,16] Recently, T_1-T_2 dual-modal contrast agents enabling both T_1 bright and T_2 dark contrasts

Received: May 15, 2019
Published: May 22, 2019

DOI: 10.1021/acs.bioconjchem.9b00349
Bioconjugate Chem. 2019, 30, 1821−1829

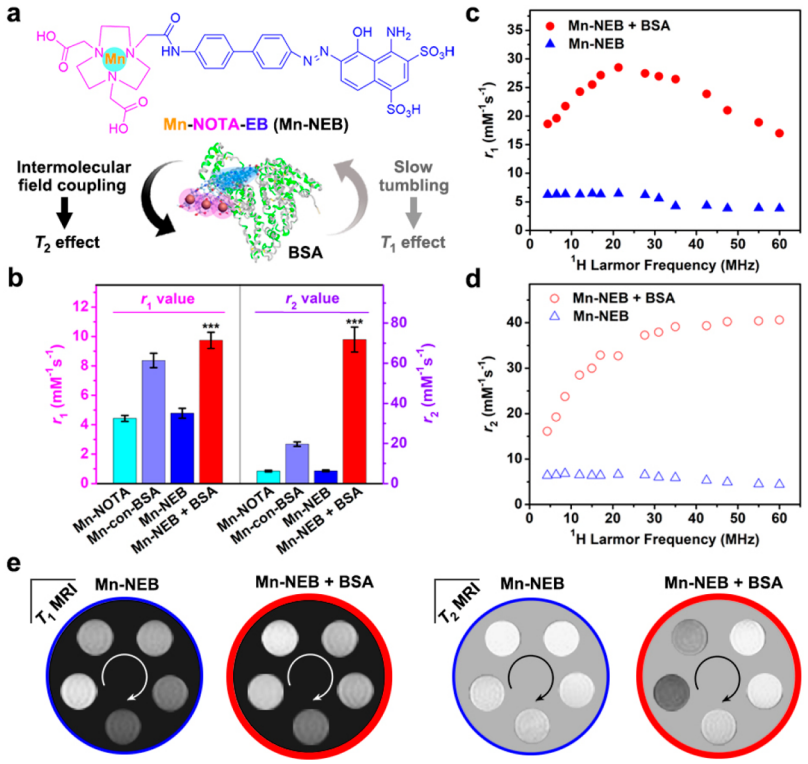

Figure 1. Protein binding complexes as T_1-T_2 dual-modal MRI contrast agents. (a) Chemical structure of the Mn-NEB. The intermolecular magnetic field coupling and slow tumbling feature of Mn-NEB + BSA lead to T_1 and T_2 relaxation enhancement. (b) Column shows the r_1 and r_2 values of Mn-NOTA, Mn-con-BSA, and Mn-NEB with or without BSA, measured at 7 T. ***$P < 0.001$. (c, d) The T_1 and T_2 nuclear magnetic resonance dispersion (NMRD) profiles of the Mn-NEB in the presence (red) and absence (blue) of BSA. (e) Representative T_1 and T_2 MRI phantoms of Mn-NEB at different concentrations with or without BSA. The circular arrows from start to end indicate Mn concentrations from high to low (1, 0.5, 0.25, 0.125, and 0 mM).

have gained momentum.[17,18] Traditional paramagnetic molecules have T_1 contrast ability but negligible T_2 contrast even though the r_2 relaxivity value is still higher than the r_1 value.[19,20] The T_1 relaxivity of paramagnetic molecules can be enhanced by formation of macromolecules (e.g., binding with proteins).[21,22] However, the change in T_2 relaxivity was often ignored. The T_2 relaxivity can be modulated by regulating the intermolecular magnetic field coupling of the magnetic centers.[23,24] On this occasion, paramagnetic molecules may serve as T_1-T_2 dual-modal MRI through structural engineering.[25] The use of T_1-T_2 dual-modal contrast agents can generate comparative images with the same in-plane geometries but with different contrasts, which hold great promise in self-confirmed MRI detection with improved accuracy and precision.[17,18] However, conventional signal intensity-based MRI are still limited to their semiquantitative nature, which is susceptible to many factors such as tissue type and scanner.[26] Lesion detection in conventional MRI depends on subjective interpretation of signal appearance and contrast in the MR images. Recently, the T_1 and T_2 mapping strategy has aroused increasing interest because of the merits of quantitative evaluation of the T_1 and T_2 relaxation times in tissues.[27−30] For example, quantitative MRI has found great utility in precision diagnosis of clinically occult diseases with a dispersive and infiltrative nature, such as cardiovascular and brain abnormalities.[31,32]

Herein, we studied a laboratory-made 1,4,7-triazacyclononane-*N*,*N*′,*N*″-triacetic acid (NOTA) conjugated truncated Evans blue (NEB),[33] after chelating with manganese ion (Mn-NEB) and binding with bovine serum albumin (Mn-NEB + BSA), as novel T_1-T_2 dual-modal MRI contrast agents. Furthermore, the T_1-T_2 dual-modal MRI and postimaging computations on T_1 and T_2 relaxation time changes were evaluated as a new paradigm of MRI for tumor imaging. Because both T_1 and T_2 maps can be acquired with an exact match of the in-plane geometry, this method is able to generate a single picture integrating the quantitative T_1 and T_2 relaxation changes (e.g., $\Delta R_1 \times \Delta R_2$) with improved signal-to-noise ratios (SNR) and contrast-to-noise ratios (CNR).

RESULTS AND DISCUSSION

An Albumin-Binding Molecule as T_1-T_2 Dual-Modal MRI Contrast Agent. Evans blue (EB) dye has been widely used in clinical practices due to the ability of binding to serum albumin with high affinity and a long blood half-life in vivo.[33] Previously, our group has developed a series of EB derivatives with different functional attachments for long-acting therapeutics and diagnostic imaging.[33−35] In this work, we studied Mn-NEB as MRI contrast agents through binding with BSA, where the EB motifs form a stacking structure in the cleft of BSA. It is well-documented that the slow tumbling feature of the Mn-NEB + BSA can result in enhanced T_1 effect (Figure 1a). Notably, the intermolecular field coupling of magnetic centers (i.e., Mn^{2+}) may cause augmented local field inhomogeneity which leads to enhanced T_2 relaxivity.[36]

The results showed that Mn-NEB + BSA has an outstanding r_1 value of 9.74 ± 0.55 mM^{-1} s^{-1} at 7 T (Figure 1b), whereas Mn-NOTA, Mn covalently conjugated BSA (Mn-con-BSA), and Mn-NEB only showed r_1 values of 4.43 ± 0.2, 8.37 ± 0.49, and 4.78 ± 0.34 mM^{-1} s^{-1}, respectively. The high r_1 values of

DOI: 10.1021/acs.bioconjchem.9b00349
Bioconjugate Chem. 2019, 30, 1821−1829

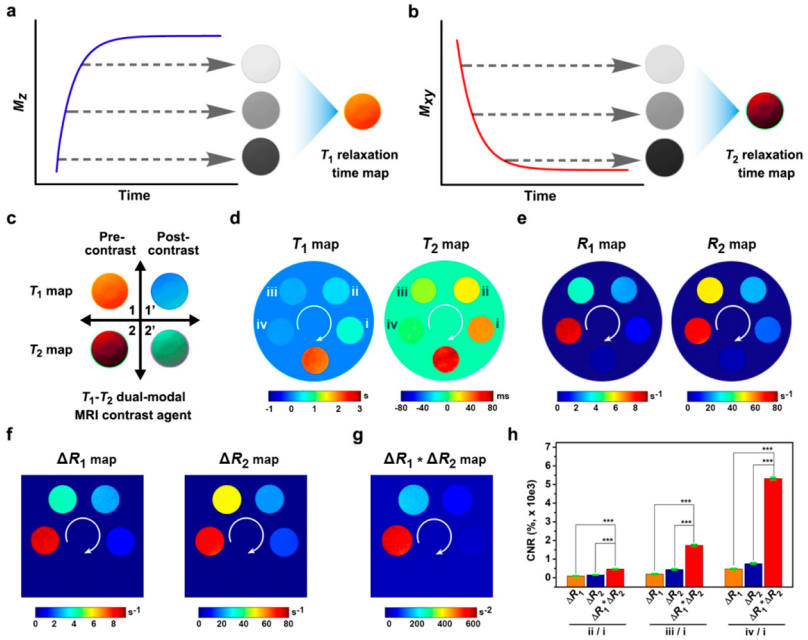

Figure 2. Phantom analysis of orthogonal computations on T_1−T_2 dual-modal MRI. (a,b) Illustration of T_1 recovery and T_2 decaying signals and imaging appearance at different acquisition times, which can be fitted into the curve for simulating T_1 and T_2 relaxation time maps, respectively. (c) Scheme shows the logic of pre- and postcontrast T_1−T_2 dual-modal MRI (1 vs 1', 2 vs 2'). The color intensity indicates the quantitative T_1 and T_2 relaxation times. (d) The T_1 and T_2 relaxation time maps of Mn-NOTA + BSA samples in phantom with different concentrations. The circular arrows from start to end indicate Mn concentrations from high to low (denoted as iv, iii, ii, and i), representing 1, 0.5, 0.25, 0.125, and 0 mM. (e) The R_1 and R_2 maps conducted from the numerical reciprocals of the corresponding T_1 and T_2 relaxation time maps in d. (f) The ΔR_1 and ΔR_2 maps obtained from e by numerical subtracting the background (0 mM) for each concentrations (i–iv), which were then used to generate the ΔR_1 * ΔR_2 map (g). (h) Quantification of CNR for the ΔR_1, ΔR_2, and ΔR_1 * ΔR_2 maps. The CNR represents the contrast agents at high concentrations (ii, iii, and iv as contrast) to that of low concentration (i as noise). ***P < 0.001.

the Mn-con-BSA and Mn-NEB + BSA are both attributed to the slow tumbling feature of BSA compared with that of Mn-NOTA molecules.[37] The intermolecular field coupling effect in the Mn-NEB + BSA is revealed by the outperformed r_2 value of 71.8 ± 6.2 mM^{-1} s^{-1} which is 3.6-fold higher than that of Mn-con-BSA (19.68 ± 1.1 mM^{-1} s^{-1}), in which their r_1 values are comparable (Table S1). The albumin binding status of Mn-NEB was further confirmed by the gel electrophoresis analysis (Figure S1).

We measured the T_1 and T_2 nuclear magnetic resonance dispersion (NMRD) profiles of the Mn-NEB in the presence and absence of BSA. A "hump" at proton Larmor frequency around 20 MHz was found for the T_1 NMRD curve of Mn-NEB + BSA, indicating the formation of slow tumbling protein complexes (Figure 1c). The T_1 relaxation values for the Mn-NEB + BSA are greatly higher than those of Mn-NEB itself with the ^{1}H Larmor frequency ranging from 4 to 60 MHz, which can be ascribed to the enhanced inner-sphere relaxivity. The T_2 NMRD profiles of Mn-NEB + BSA showed higher T_2 relaxivity values at different fields compared with those of Mn-NEB itself (Figure 1d). It is noteworthy that the enhanced T_2 relaxivity becomes more significant at higher magnetic field. The representative T_1 and T_2 weighted phantom of Mn-NEB with or without BSA at different concentrations were shown (Figure 1e). The concentration range is 1 to 0.5, 0.25, 0.125, and 0 mM (circular arrow, from start to end). The enhanced contrast in both T_1 and T_2 phantoms of Mn-NEB + BSA compared with that of Mn-NEB only are consistent with the r_1 and r_2 values above. On the contrary, the phantom contrast for Mn-NOTA in the presence or absence of BSA shows little difference (Figure S2). These results suggest that the Mn-NEB + BSA complex is a good candidate for T_1−T_2 dual-modal MRI due to intermolecular field coupling and slow tumbling features.

Computations on T_1−T_2 Dual-Modal MRI. Proton magnetization during the relaxation recovery at longitudinal (M_z) direction or decaying at transverse (M_{xy}) plane is both time-dependent, which is the source of bright/dark signal for the respective T_1 and T_2 images. Therefore, the acquired MR images at different time points along with a relaxation time period can be fitted in line, which are then simulated into a single map representing the voxel-by-voxel T_1 or T_2 relaxation times (Figure 2a,b). By using T_1−T_2 dual-modal MRI contrast agents, it is expected that both T_1 and T_2 maps at precontrast and postcontrast can be obtained (Figure 2c). We conducted the T_1 and T_2 phantom maps according to 7 and 16 multiparameter images, respectively, with different concentrations of Mn-NEB + BSA samples, from 1 to 0.5, 0.25, 0.125, and 0 mM (circular arrow, from start to end) (Figure 2d and Figure S3). The pseudocolor intensity in these maps represents the T_1 or T_2 relaxation time, which is exclusively related to the physicochemical properties (e.g., chemical environment, physical states) of imaging targets at a given magnetic field. More importantly, the relaxation maps benefit further numerical computing and analysis, which is an explicit advance to conventional semiquantitative signal intensity-based MRI analysis.

To further demonstrate this feasibility, we converted the T_1 and T_2 maps into R_1 ($1/T_1$) and R_2 ($1/T_2$) phantom maps (Figure 2e). We defined the specimen of H_2O (0 mM) as precontrast sample, and the others containing contrast agents are postcontrast samples. In the first step, we conducted

DOI: 10.1021/acs.bioconjchem.9b00349
Bioconjugate Chem. 2019, 30, 1821−1829

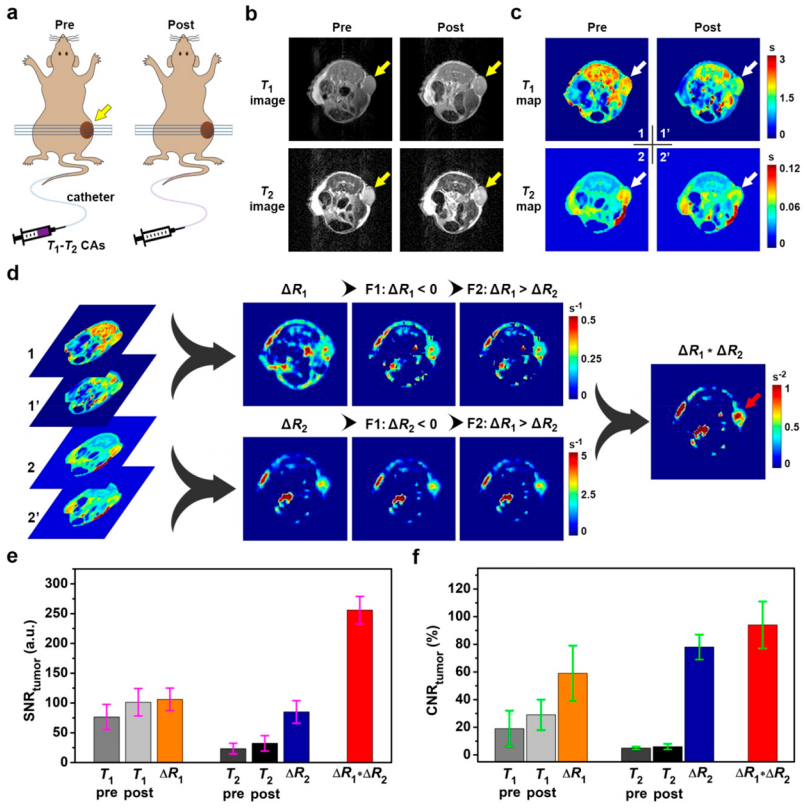

Figure 3. Orthogonal computations on T_1−T_2 dual-modal MRI of subcutaneous tumor model. (a) Illustration of acquisition of pre- and postcontrast T_1−T_2 dual-modal MRI with the same in-plane slices through a prefixed catheter for intravenous injection of contrast agents. (b) Representative T_1- and T_2-weighted images at pre- and postcontrast time points. These images were acquired at the same in-plane axial slices with tumor (yellow arrow). (c) The T_1 and T_2 relaxation time maps for the pre- (1 and 2) and postcontrast (1' and 2') points of the imaging slice shown in b. (d) The ΔR_1 and ΔR_2 maps were obtained from numerical subtraction of postcontrast R_1 and R_2 maps by precontrast R_1 and R_2 maps, respectively. The ΔR_1 and ΔR_2 maps were then deduced by two logic filters (F1: $\Delta R_1 < 0$, $\Delta R_2 < 0$; F2: $\Delta R_1 > \Delta R_2$) to filter out false-positive relaxation changes on the maps, which were then used for generating $\Delta R_1 * \Delta R_2$ map. (e, f) Quantification of SNR (e) and CNR (f) of the subcutaneous tumor for the T_1 and T_2 weighted images, ΔR_1, ΔR_2, and $\Delta R_1 * \Delta R_2$ maps. Values are presented as mean ± SD.

computation of ΔR ($R_{postcontrast} - R_{precontrast}$) on both R_1 and R_2 maps, in which the color intensity implies the ability of contrast agents in altering proton relaxations at different concentrations (Figure 2f). We then used multiplication ($\Delta R_1 \times \Delta R_2$) to combine the T_1 and T_2 relaxation changes for each of the corresponding concentrations of contrast agents (Figure 2g). Previous publications regarding the calculation of SNR were mainly based on the signal intensity analysis of black-and-white MR images according to a single-image measurement procedure provided by the National Electrical Manufacturers Association (NEMA) standards (MS 6-2008, R2014). In our case, the color intensity on relaxation map represents quantitative voxel-by-voxel relaxation times. Therefore, we adjusted the traditional method of assessing SNR and CNR to the use of quantitative relaxation values for the ΔR_1, ΔR_2, and $\Delta R_1 \times \Delta R_2$ maps of the Mn-NEB + BSA. It is noteworthy that the multiplication on ΔR_1 and ΔR_2 maps would also enhance the background noise in the final outputs(Figure S4 and S5). However, quantification analysis results show that the CNR for those high concentrations (ii, iii, iv) to the lowest concentration (i) were significantly enhanced (***P < 0.001) for the $\Delta R_1 \times \Delta R_2$ map compared with those of either single ΔR_1 or ΔR_2 map (Figure 2h). More importantly, the numerical deduction of relaxation changes may provide a new paradigm to evaluate MRI contrast agents or follow-up diagnosis of histological changes in diseases in a quantitative manner.

Computations on In Vivo MRI of Subcutaneous Tumors. To evaluate the feasibility of T_1−T_2 computations *in vivo*, we performed T_1−T_2 dual-modal MRI in a subcutaneous mouse tumor model. The multiparametric T_1 and T_2 images were acquired before (precontrast) and after (postcontrast) intravenous injection of Mn-NEB through a prefixed catheter (Figure 3a and Figure S6). In this way, we are able to analyze the T_1−T_2 weighted images and the corresponding T_1 and T_2 relaxation maps under the same in-plane geometries. In Figure 3b, we showed two pairs of typical T_1 and T_2 weighted images at pre- and postcontrast of an axial slice of tumor (yellow arrow). It is worth noting that the signal intensity on each MRI weighted image is expressed as arbitrary unit which hampers directly compare those pre- and postcontrast images. By constructing T_1 and T_2 relaxation time maps, the appearance of voxel-by-voxel color intensity reveals distinct information on the heterogeneous distribution of relaxation times within the tumor (Figure 3c). The heterogeneous changes of the relaxation times in the T_1 and T_2 maps were also observed, indicating different accumulation of the contrast agents in the tumor (1 vs 2; 1' vs 2').

Furthermore, we conducted numerical computations on those relaxation time maps to yield ΔR_1 and ΔR_2 maps (Figure 3d). Before applying the computations, we performed two

DOI: 10.1021/acs.bioconjchem.9b00349
Bioconjugate Chem. 2019, 30, 1821−1829

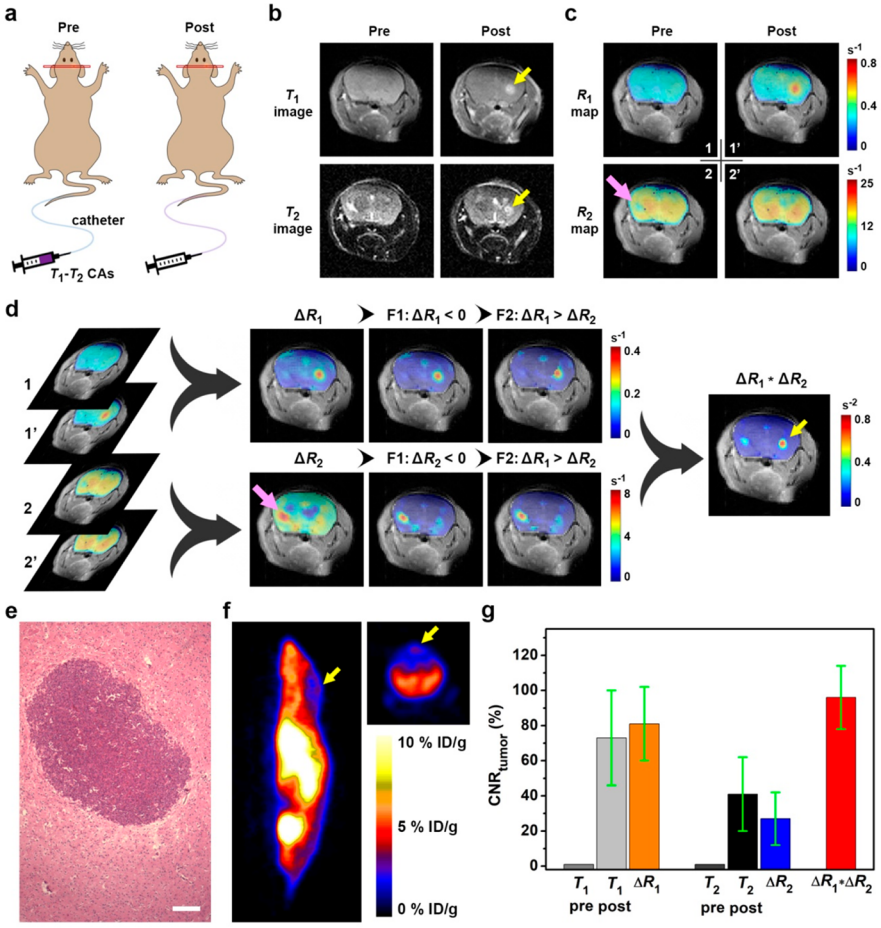

Figure 4. Orthogonal computations on T_1−T_2 dual-modal MRI of orthotopic brain tumor model. (a) Illustration of acquisition of pre- and postcontrast T_1−T_2 dual-modal MRI with the same in-plane slices through a prefixed catheter for intravenous injection of contrast agents. (b) Representative T_1- and T_2-weighted images of mouse brain at pre- and postcontrast points. Yellow arrows indicate hyperintense foci in the brain. (c) The R_1 and R_2 maps for the pre- (1 and 2) and postcontrast (1' and 2') points of the imaging slice shown in b. (d) The ΔR_1 and ΔR_2 maps were obtained from numerical subtraction of postcontrast R_1 and R_2 maps by precontrast R_1 and R_2 maps, respectively. The ΔR_1 and ΔR_2 maps were then deduced by two logic filters (F1: $\Delta R_1 < 0$, $\Delta R_2 < 0$; F2: $\Delta R_1 > \Delta R_2$) to filter out false-positive relaxation changes on the maps, which were then used for generating $\Delta R_1 * \Delta R_2$ map. Pink arrow shows suspicious relaxation change possibly from the CSF flow. Yellow arrow indicates the hyperintense foci. (e) H&E staining of mouse brain slice showing the presence of brain tumor. (f) PET images of mouse with brain tumor (yellow arrow). Scale bar: 100 μm. (g) Quantification of CNR of the brain tumor for the T_1 and T_2 weighted images, ΔR_1, ΔR_2, and $\Delta R_1 * \Delta R_2$ maps. Values are presented as mean ± SD.

logic filters on the obtained ΔR_1 and ΔR_2 maps to eliminate potential imaging artifacts. The first filter, $\Delta R_1 < 0$ and $\Delta R_2 < 0$, is based on the fact that MRI contrast agents are responsible for acceleration of the relaxation processes or reduction of relaxation times. The second filter, $\Delta R_1 > \Delta R_2$, is based on that T_1 relaxation time is always longer than T_2 relaxation time for a given subject. As a result, these filters help remove considerable volume of artifacts or false-positive signals on both ΔR_1 and ΔR_2 maps. At the end, the final output $\Delta R_1 \times \Delta R_2$ map shows a conspicuous contrast for ROI of tumor (red arrow) with little neighboring background. Furthermore, we analyzed the semiquantitative signal changes of the pre- and postcontrast T_1 and T_2 weighted images compared with those of the ΔR_1, ΔR_2, and $\Delta R_1 \times \Delta R_2$ maps (Figure 3e,f). The results reveal that the T_1−T_2 MRI contrast agents delivered marginal enhancement to T_1 and T_2 weighted images with little changes on SNR and CNR of the tumor, likely due to the limited accumulation of contrast agents in the tumor. On the contrary, both SNR and CNR were remarkably enhanced for the ΔR_2 map compared with the T_2 weighted images, whereas the ΔR_1 map revealed very shallow enhancement probably due to the presence of artifacts and false-positive signals. The notable enhancement of SNR and CNR was recorded for the $\Delta R_1 \times \Delta R_2$ map compared with any single weighted images or ΔR maps. These results imply that the computations integrating both T_1 and T_2 relaxation changes assisted by T_1−T_2 dual-modal contrast agents can augment the ability of lesion detection *in vivo*, compared with traditional MRI diagnosis based on signal-intensity changes of weighted images.

Computations on MRI of Orthotopic Brain Tumors. Glioblastoma is a highly aggressive and lethal type of brain cancer. MRI is one of the most widely used imaging modalities for the detection of gliomas in clinic due to the excellent soft tissue contrast. However, the dispersive and infiltrative natures of gliomas within brain as well as the complexity of brain structures make the visualization of gliomas particularly challenging. Although MRI contrast agents could provide enhanced tumor-to-background contrast, traditional imaging strategies are naturally qualitative and require subjective interpretation on the weighted images. We anticipated that

DOI: 10.1021/acs.bioconjchem.9b00349
Bioconjugate Chem. 2019, 30, 1821−1829

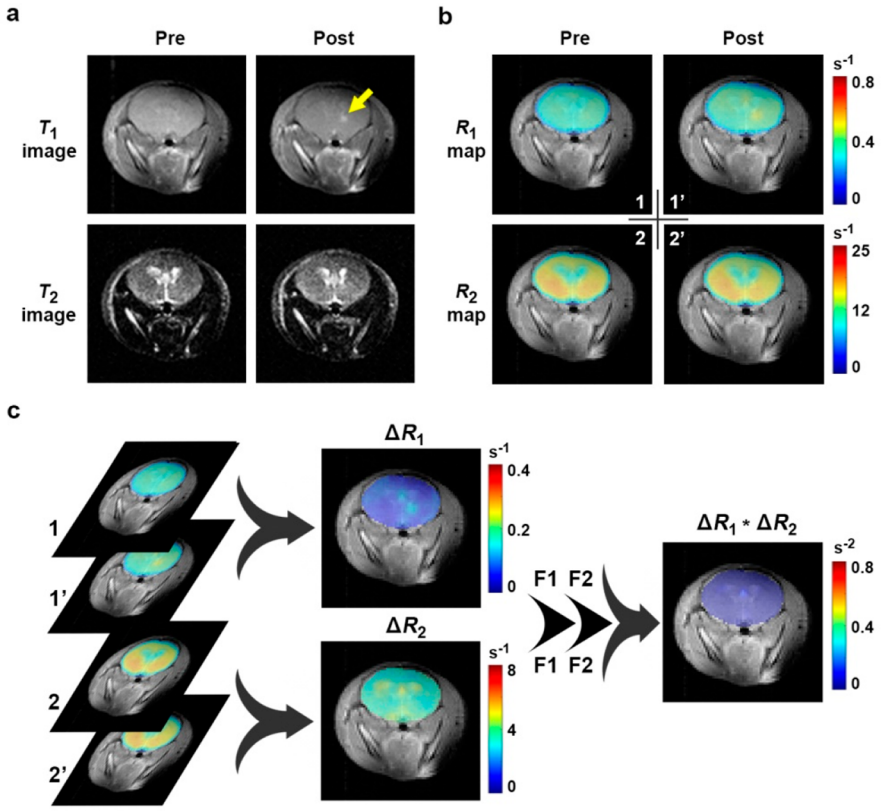

Figure 5. Orthogonal computations eliminate false-positive diagnosis in brain imaging. (a) Representative T_1- and T_2-weighted images of mouse brain at pre- and postcontrast points, acquired at the same in-plane slices. Yellow arrows indicate hyperintense foci in the brain. (b) The conducted R_1 and R_2 maps for the pre- (1 and 2) and postcontrast (1' and 2') points of the imaging slice shown in b. (c) The numerical conduction (ΔR_1 and ΔR_2), logic filtering (F1 and F2), and orthogonal computations on the T_1 and T_2 relaxation maps yield ΔR_1 * ΔR_2 map showing no indication of hyperintense foci.

the computations based on T_1-T_2 dual-modal MRI may offer new opportunities for precision detection of gliomas. As above-described, T_1 and T_2 weighted images at pre- and postcontrast of mouse brain were acquired with the same in-plane geometries (Figure 4a). Because of the accumulation of intravenously injected Mn-NEB contrast agents, a clear shape of lesion (yellow arrow) appeared at the postcontrast images, which was not obvious at the precontrast images (Figure 4b). It is interesting that the postcontrast T_2 weighted image also appears a bright contrast in the brain, which could be due to the low amount of accumulated contrast agents in tumor. As a result, the T_1 recovery effect at low concentration of contrast agents contributes to the bright signal output. It is noteworthy that the imaging appearance is also dependent on the parameter settings on different imaging sequences.

Subsequently, we reconstructed the T_1 and T_2 weighted images acquired from mapping sequences into R_1 and R_2 numerical maps (Figure 4c and Figure S7). In these maps, the postcontrast R_1 map displayed good contrast for the hyperintense foci; however, a relatively high background signal was also recorded. We then conducted numerical computations individually and applied two logic filters to the ΔR_1 and ΔR_2 maps (Figure 4d). It was found that the ΔR_2 map showed another suspicious hypointense foci in the brain (pink arrow), which was remaining after two logic filters. This phenomenon together with the high occurrence of artifacts are representative characters of brain due to the complex networks and the presence of dynamic CSF flow in brain, which greatly dampens the ability of precision diagnosis in MRI. In this respect, we conducted the computation to generate $\Delta R_1 \times \Delta R_2$ map of the brain MRI, which showed a great contrast for the hyperintense foci in the brain with diminished artifacts and background signals. Meanwhile, signal contrast for the suspicious foci was on the contrary clearly diminished after the T_1-T_2 computations.

The existence of mouse brain tumor was confirmed by hematoxylin and eosin (H&E) staining of the dissected brain slices (Figure 4e). The H&E experiments also verified that only one tumor was found in the mouse brain, implying that the suspicious hypointense foci observed on the ΔR_2 map above was a false-positive signal. In fact, the false-positive signal change was not observed in the imaging results of an adjacent slice which were acquired under the same imaging courses (Figure S8). We further used PET to inspect the brain imaging results by MRI, in which ^{68}Ga-radiolabeled NEB was employed according to our reported procedures.[34] The PET images showed that the brain tumor had a gradually increased mean tumor uptake of 1.43%, 3.08%, and 3.26% ID% g^{-1} at the 30, 60, and 90 min postinjection time-points (Figure 4f and Figure S9). The PET results also showed that the mouse brain area other than the tumor had little to no signals possibly because of the remaining intact blood-brain barrier. Numerical analysis of the imaging results showed that the T_1-T_2 dual-modal contrast agents could greatly enhance the SNR and CNR of mouse brain tumor which was virtually undetectable in the precontrast MRI (Figure 4g and Figure S10). The ΔR_1 and ΔR_2 maps before applying logic filters showed little increased or even lower SNR and CNR, which could be due to

DOI: 10.1021/acs.bioconjchem.9b00349
Bioconjugate Chem. 2019, 30, 1821−1829

the interference from artifacts and/or false-positive signal. However, the combination of T_1 and T_2 relaxation changes using computation ($\Delta R_1 \times \Delta R_2$) leads to distinctly higher SNR and CNR compared with those of either T_1 or T_2 model.

Computations Help Eliminate False-Positive Diagnosis in Brain Imaging. Previous results suggest that the postimaging computation method can enhance the SNR and CNR in lesion detection, especially in brain imaging. In our experiments, we also found that the T_1-T_2 dual-modal MRI computation method was able to eliminate false positive diagnosis in a tumor-free mouse brain MRI study. As shown in Figure 5a, the postcontrast T_1 weighted image displayed a hyperintense foci in the brain (white arrow), which could have led to a false-positive diagnosis of brain tumor. However, the signal change in postcontrast T_2 weighted image was marginal, which complicated the diagnostic assessment. We then fitted T_1 and T_2 weighted images to generate R_1 and R_2 maps (Figure 5b and Figure S11). The comparative analysis of the pre- and postcontrast R_1 and R_2 maps seems to be difficult due to the highly dispersive signals in the brain. The computations by $\Delta R_1 \times \Delta R_2$ equipped with logic filters eliminated the hyperintense foci which is potentially a false-positive signal (Figure 5c). The H&E staining experiments confirmed the absence of brain tumor (results not shown). This result implies that the signal changes observed in the T_1 weighted images have high propensity to be interfered by false-positive interference, which is technically difficult to avoid because of the presence of CSF and/or blood flow in the brain. In this respect, our method may provide a more advanced imaging strategy to reduce diagnostic uncertainty in diagnosing brain diseases using MRI.

CONCLUSIONS

In summary, we developed an albumin-binding T_1-T_2 dual-modal MRI contrast agent for postimaging computations integrating both T_1 and T_2 relaxation changes. The quantitative computations on T_1-T_2 dual-modal MRI lead to enhanced SNR and CNR of tumors demonstrated in both subcutaneous xenograft and orthotopic brain tumor models, indicating great feasibility in precision diagnosis. Moreover, we showed that this method could help eliminate suspicious artifacts and false-positive signals in tumor-free mouse brain MRI. It is noteworthy that the postimaging computations on T_1-T_2 dual-modal MRI may be applicable to any contrast agents with justifiable T_1 and T_2 relaxivities. This study may provide insight in the paradigm of T_1-T_2 dual-modal MRI and holds great potential for precision diagnosis of clinically occult diseases.

EXPERIMENTAL SECTION

Preparation of Mn-NEB + BSA. In a typical procedure, 1654 μg of NEB (2 μmol) was dissolved in 1 mL of sodium acetate buffer (pH 5.5) to give a 2 mM solution. One milliliter of $MnCl_2$ (2 mM) buffer solution was then mixed with the 1 mL of NEB (2 mM) solution and left on vortex mixer for 10 min. The mixed solution was used for preparation of Mn-NEB + BSA molecule−protein complexes by directly mixing with 5-fold excess amount of BSA solution in phosphate buffered saline (pH 7.0). The solution was halfway diluted to give a range of Mn-NEB + BSA solutions with a concentration gradient. The NMRD profiles were recorded using the prepared Mn-NEB + BSA solution with concentration of 1 mM with respect to Mn-NEB. The solution the same concentration of Mn-NEB (1 mM) but without BSA was also prepared for comparison purpose.

MRI Measurements. The MRI phantom study was conducted on a 7 T scanner using T_1 and T_2 mapping sequences, rapid acquisition with relaxation enhancement with variable repetition time (RARE-VTR) and multislice multiecho (MSME), respectively. The phantom samples with different concentrations of Mn-NEB, Mn-NEB + BSA, Mn-NOTA, and Mn-NOTA + BSA were prepared and studied by T_1 and T_2 MRI in parallel for comparison purpose. The T_1 phantom MRI acquisition used the following parameters: Echo Time = 12.507 ms, Effective TE = 12.507 ms, Number of Experiments = 7, Multiple Repetition Time = 50, 250, 500, 1000, 2000, 4000, 6000 ms, Rare Factor = 2, Number of Averages = 2, Number of Repetitions = 1, Flip Angle = 180, Matrix = 128 × 128. Scan Time = 29 min 26 s 400 ms. The T_2 phantom MRI acquisition used the following parameters: Echo Time = 10 ms, Effective TE = 10, 20, 30, 40, 50, 60, 70, 80, 90, 100, 110, 120, 130, 140, 150, 160 ms, Repetition Time = 2000 ms, Number of Averages = 2, Number of Repetitions = 1, Flip Angle = 180, Matrix = 128 × 128. Scan Time = 6 min 24 s 0 ms.

***In Vivo* MRI of Mouse Subcutaneous Tumor.** The *in vivo* MRI of subcutaneous tumor mouse was conducted by a 7 T scanner (Bruker). We used a prefixed catheter in the mouse tail vein to acquire pre- and postcontrast T_1 and T_2MRI, respectively. After sequential scanning of precontrast T_1 and T_2 weighted MRI using the same in-plane geometries, we injected Mn-NEB intravenously from outside the scanner, while the mouse was kept anesthetized and left steady. The injection dose of Mn-NEB was 10 μmol/kg (Mn ions to mouse body weight). At 1 h postinjection time, we acquired the postcontrast T_1 and T_2 weighted MRI using the same sequence parameters and in-plane settings as those for precontrast T_1 and T_2 weighted MRI, respectively. The imaging sequence for T_1 weighted MRI was RARE-VTR pulse using the following parameters: Echo Time = 11.507 ms, Effective TE = 11.507 ms, Rare Factor = 2, Flip Angle = 180, Number of Experiments = 6, Multiple Repetition Time = 302, 500, 1000, 2000, 4000, 6000 ms, Number of Averages = 2, Number of Repetitions = 1, Matrix = 128 × 128. Scan Time = 29 min 26 s 656 ms. The T_2 weighted MRI used MSME sequence with the following parameters: Echo Time = 11 ms, Repetition Time = 2000 ms, Effective TE = 11, 22, 33, 44, 55, 66, 77, 88, 99, 110, 121, 132, 143, 154, 165, 176 ms, Rare Factor = 2, Number of Averages = 2, Number of Repetitions = 1, Flip Angle = 180, Matrix = 128 × 128. Scan Time = 8 min 32 s 0 ms.

***In Vivo* MRI of Orthotopic Mouse Brain Tumor.** For brain MRI study, we used the prefixed catheter setups as described above to acquire pre- and postcontrast T_1 and T_2 weighted MRI data, respectively. A mouse-specific head coil was used in all brain MRI experiments. After sequential scanning of precontrast T_1 and T_2 weighted MRI data using the same in-plane geometries, we injected Mn-NEB intravenously from outside the scanner while the mouse was kept anesthetized and left steady. The injection dose was 10 μmol/kg (Mn ions to mouse body weight). At 1 h postinjection time, we acquired the postcontrast T_1 and T_2 weighted MRI using the same sequence parameters and in-plane settings as those for precontrast T_1 and T_2 weighted MRI, respectively. The T_1 weighted MRI was acquired using RARE-VTR sequence with the following parameters: Echo Time = 12.6 ms, Effective TE = 12.6 ms, Rare Factor = 2, Flip Angle = 180, Number of

DOI: 10.1021/acs.bioconjchem.9b00349
Bioconjugate Chem. 2019, 30, 1821−1829

Experiments = 7, Multiple Repetition Time = 320, 400, 800, 1500, 2500, 4000, 6000 ms, Number of Averages = 1, Number of Repetitions = 1, Matrix = 128 × 128. Scan Time = 16 min 33 s 280 ms. The T_2 weighted MRI was acquired using MSME sequence with the following parameters: Echo Time = 11 ms, Effective TE = 11, 22, 33, 44, 55, 66, 77, 88, 99, 110, 121, 132, 143, 154, 165, 176 ms, Repetition Time = 2000 ms, Rare Factor = 2, Number of Averages = 1, Number of Repetitions = 1, Flip Angle = 180, Matrix = 128 × 128. Scan Time = 4 min 16 s 0 ms.

Computations on MRI Data. All the calculations were performed on home-written programs in MATLAB 2018a (MathWorks, Natick, MA, U.S.A.).

The quantitative T_2 maps were calculated from the multiecho signals with nonlinear least-squares fitting of the data with the following equation:

$$M(\mathrm{TE}) = M_0 \exp(-\mathrm{TE}/T_2)$$

where $M(\mathrm{TE})$ was the signal intensity at each TE and M_0 was a free fitting variable and equal to $M(\mathrm{TE} = 0)$. In the phantom experiments where the signal in some voxels reached noise floor at large TEs, the signal correction for Rician noise was performed.[38]

The quantitative T_1 maps were calculated from the multi-TR signals with nonlinear least-squares fitting of the data with the following equation:

$$M(\mathrm{TR}) = M_0\left(1 - \exp\left(-\frac{\mathrm{TR}}{T_1}\right)\right)$$

where $M(\mathrm{TR})$ was the signal intensity at each TR and M_0 was a free fitting variable and equal to $M(\mathrm{TR} = +\mathrm{inf})$.

■ ASSOCIATED CONTENT

Supporting Information

The Supporting Information is available free of charge on the ACS Publications website at DOI: 10.1021/acs.bioconjchem.9b00349.

Supplementary methods and additional data as noted in the text (PDF)

■ AUTHOR INFORMATION

Corresponding Authors

*E-mail: ruiliangbai@zju.edu.cn.
*E-mail: jhgao@xmu.edu.cn.
*E-mail: shawn.chen@nih.gov.

ORCID

Longguang Tang: 0000-0002-9517-1325
Jinhao Gao: 0000-0003-3215-7013
Xiaoyuan Chen: 0000-0002-9622-0870

Notes

The authors declare no competing financial interest.

■ ACKNOWLEDGMENTS

This work was supported by the Intramural Research Program (IRP), National Institute of Biomedical Imaging and Bioengineering (NIBIB), National Institutes of Health (NIH), and by the National Science Foundation of China (81873894, 21771148 and 21521004). We thank Ms. Danielle Donahue and Ms. Vivian Diaz for helping setup animal data acquisitions.

■ REFERENCES

(1) Aguado, B. A., Grim, J. C., Rosales, A. M., Watson-Capps, J. J., and Anseth, K. S. (2018) Engineering precision biomaterials for personalized medicine. *Sci. Transl. Med. 10*, No. eaam8645.
(2) Ehlerding, E. B., and Cai, W. (2016) Harnessing the power of molecular imaging for precision medicine. *J. Nucl. Med. 57*, 171−172.
(3) Kim, M. M., Parolia, A., Dunphy, M. P., and Venneti, S. (2016) Non-invasive metabolic imaging of brain tumours in the era of precision medicine. *Nat. Rev. Clin. Oncol. 13*, 725.
(4) Gambhir, S. S. (2002) Molecular imaging of cancer with positron emission tomography. *Nat. Rev. Cancer 2*, 683.
(5) Cassat, J. E., Moore, J. L., Wilson, K. J., Stark, Z., Prentice, B. M., Van de Plas, R., Perry, W. J., Zhang, Y., Virostko, J., Colvin, D. C., et al. (2018) Integrated molecular imaging reveals tissue heterogeneity driving host-pathogen interactions. *Sci. Transl. Med. 10*, No. eaan6361.
(6) Patel, R., Khan, A., Quinlan, R., and Yaroslavsky, A. N. (2014) Polarization-sensitive multimodal imaging for detecting breast cancer. *Cancer Res. 74*, 4685−4693.
(7) Teipel, S., Drzezga, A., Grothe, M. J., Barthel, H., Chételat, G., Schuff, N., Skudlarski, P., Cavedo, E., Frisoni, G. B., Hoffmann, W., et al. (2015) Multimodal imaging in alzheimer's disease: Validity and usefulness for early detection. *Lancet Neurol. 14*, 1037−1053.
(8) Moseley, M., and Donnan, G. (2004) Multimodality imaging. *Stroke 35*, 2632−2634.
(9) Boeve, B. F., and Kantarci, K. (2018) Multimodal imaging in rbd — present and future. *Nat. Rev. Neurol. 14*, 574−576.
(10) Pagel, M. D. (2011) The hope and hype of multimodality imaging contrast agents. *Nanomedicine 6*, 945−948.
(11) Fjell, A. M., Walhovd, K. B., Brown, T. T., Kuperman, J. M., Chung, Y., Hagler, D. J., Venkatraman, V., Roddey, J. C., Erhart, M., McCabe, C., et al. (2012) Multimodal imaging of the self-regulating developing brain. *Proc. Natl. Acad. Sci. U. S. A. 109*, 19620−19625.
(12) Vandenberghe, S., and Marsden, P. K. (2015) PET-MRI: A review of challenges and solutions in the development of integrated multimodality imaging. *Phys. Med. Biol. 60*, R115.
(13) Weissman, N. J., Soman, P., and Shah, D. J. (2013) Multimodality imaging: Opportunities and challenges. *JACC: Cardiovasc. Imaging 6*, 1022−1023.
(14) Akazawa, K., Sugihara, F., Nakamura, T., Matsushita, H., Mukai, H., Akimoto, R., Minoshima, M., Mizukami, S., and Kikuchi, K. (2018) Perfluorocarbon-based 19F MRI nanoprobes for in vivo multicolor imaging. *Angew. Chem., Int. Ed. 57*, 16742−16747.
(15) Pierre, V. C., Harris, S. M., and Pailloux, S. L. (2018) Comparing strategies in the design of responsive contrast agents for magnetic resonance imaging: A case study with copper and zinc. *Acc. Chem. Res. 51*, 342−351.
(16) Ni, D., Bu, W., Ehlerding, E. B., Cai, W., and Shi, J. (2017) Engineering of inorganic nanoparticles as magnetic resonance imaging contrast agents. *Chem. Soc. Rev. 46*, 7438−7468.
(17) Shin, T. H., Choi, J. S., Yun, S., Kim, I. S., Song, H. T., Kim, Y., Park, K. I., and Cheon, J. (2014) T_1 and T_2 dual-mode MRI contrast agent for enhancing accuracy by engineered nanomaterials. *ACS Nano 8*, 3393−3401.
(18) Zhou, Z., Bai, R., Munasinghe, J., Shen, Z., Nie, L., and Chen, X. (2017) T1-T2 dual-modal magnetic resonance imaging: From molecular basis to contrast agents. *ACS Nano 11*, 5227−5232.
(19) Werner, E. J., Datta, A., Jocher, C. J., and Raymond, K. N. (2008) High-relaxivity MRI contrast agents: Where coordination chemistry meets medical imaging. *Angew. Chem., Int. Ed. 47*, 8568−8580.
(20) Keca, J. M., Chen, J., Overchuk, M., Muhanna, N., MacLaughlin, C. M., Jin, C. S., Foltz, W. D., Irish, J. C., and Zheng, G. (2016) Nanotexaphyrin: One-pot synthesis of a manganese texaphyrin-phospholipid nanoparticle for magnetic resonance imaging. *Angew. Chem., Int. Ed. 55*, 6187−6191.
(21) Caravan, P. (2006) Strategies for increasing the sensitivity of gadolinium based MRI contrast agents. *Chem. Soc. Rev. 35*, 512−523.

DOI: 10.1021/acs.bioconjchem.9b00349
Bioconjugate Chem. 2019, 30, 1821−1829

(22) Caravan, P., Greenfield, M. T., Li, X., and Sherry, A. D. (2001) The Gd^{3+} complex of a fatty acid analogue of DOTA binds to multiple albumin sites with variable water relaxivities. *Inorg. Chem. 40*, 6580−6587.
(23) Zhou, Z., Tian, R., Wang, Z., Yang, Z., Liu, Y., Liu, G., Wang, R., Gao, J., Song, J., Nie, L., et al. (2017) Artificial local magnetic field inhomogeneity enhances T2 relaxivity. *Nat. Commun. 8*, 15468.
(24) Xue, S., Yang, H., Qiao, J., Pu, F., Jiang, J., Hubbard, K., Hekmatyar, K., Langley, J., Salarian, M., Long, R. C., et al. (2015) Protein mri contrast agent with unprecedented metal selectivity and sensitivity for liver cancer imaging. *Proc. Natl. Acad. Sci. U. S. A. 112*, 6607−6612.
(25) Courant, T., Roullin, V. G., Cadiou, C., Callewaert, M., Andry, M. C., Portefaix, C., Hoeffel, C., de Goltstein, M. C., Port, M., Laurent, S., et al. (2012) Hydrogels incorporating gddota: Towards highly efficient dual T1/T2MRI contrast agents. *Angew. Chem., Int. Ed. 51*, 9119−9122.
(26) Kanda, T., Ishii, K., Kawaguchi, H., Kitajima, K., and Takenaka, D. (2014) High signal intensity in the dentate nucleus and globus pallidus on unenhanced T1-weighted mr images: Relationship with increasing cumulative dose of a gadolinium-based contrast material. *Radiology 270*, 834−841.
(27) Keereman, V., Fierens, Y., Broux, T., De Deene, Y., Lonneux, M., and Vandenberghe, S. (2010) MRI-based attenuation correction for PET/MRI using ultrashort echo time sequences. *J. Nucl. Med. 51*, 812−818.
(28) Mezer, A., Yeatman, J. D., Stikov, N., Kay, K. N., Cho, N.-J., Dougherty, R. F., Perry, M. L., Parvizi, J., Hua, L. H., Butts-Pauly, K., et al. (2013) Quantifying the local tissue volume and composition in individual brains with magnetic resonance imaging. *Nat. Med. 19*, 1667−1672.
(29) Deoni, S. C. L., Peters, T. M., and Rutt, B. K. (2005) High-resolution T1 and T2 mapping of the brain in a clinically acceptable time with despot1 and despot2. *Magn. Reson. Med. 53*, 237−241.
(30) Keenan, K. E., Ainslie, M., Barker, A. J., Boss, M. A., Cecil, K. M., Charles, C., Chenevert, T. L., Clarke, L., Evelhoch, J. L., Finn, P., et al. (2018) Quantitative magnetic resonance imaging phantoms: A review and the need for a system phantom. *Magn. Reson. Med. 79*, 48−61.
(31) Mavrogeni, S., Apostolou, D., Argyriou, P., Velitsista, S., Papa, L., Efentakis, S., Vernardos, E., Kanoupaki, M., Kanoupakis, G., and Manginas, A. (2017) T1 and T2 mapping in cardiology: "Mapping the obscure object of desire. *Cardiology 138*, 207−217.
(32) Geraldes, R., Ciccarelli, O., Barkhof, F., De Stefano, N., Enzinger, C., Filippi, M., Hofer, M., Paul, F., Preziosa, P., Rovira, A., et al. (2018) The current role of MRI in differentiating multiple sclerosis from its imaging mimics. *Nat. Rev. Neurol. 14*, 199.
(33) Jacobson, O., Kiesewetter, D. O., and Chen, X. (2016) Albumin-binding evans blue derivatives for diagnostic imaging and production of long-acting therapeutics. *Bioconjugate Chem. 27*, 2239−2247.
(34) Niu, G., Lang, L., Kiesewetter, D. O., Ma, Y., Sun, Z., Guo, N., Guo, J., Wu, C., and Chen, X. (2014) In vivo labeling of serum albumin for PET. *J. Nucl. Med. 55*, 1150−1156.
(35) Wang, Y., Lang, L., Huang, P., Wang, Z., Jacobson, O., Kiesewetter, D. O., Ali, I. U., Teng, G., Niu, G., and Chen, X. (2015) In vivo albumin labeling and lymphatic imaging. *Proc. Natl. Acad. Sci. U. S. A. 112*, 208−213.
(36) Hai, Z., Ni, Y., Saimi, D., Yang, H., Tong, H., Zhong, K., and Liang, G. (2019) Γ-glutamyltranspeptidase-triggered intracellular gadolinium nanoparticle formation enhances the T2-weighted MR contrast of tumor. *Nano Lett. 19*, 2428−2433.
(37) Angelovski, G. (2016) What we can really do with bioresponsive MRI contrast agents. *Angew. Chem., Int. Ed. 55*, 7038−7046.
(38) Bai, R., Koay, C. G., Hutchinson, E., and Basser, P. J. (2014) A framework for accurate determination of the T2 distribution from multiple echo magnitude MRI images. *J. Magn. Reson. 244*, 53−63.

DOI: 10.1021/acs.bioconjchem.9b00349
Bioconjugate Chem. 2019, 30, 1821−1829